Advanced Quantum Technologies

ADVANCED QUANTUM TECHNOLOGIES
www.advquantumtech.com

RESEARCH ARTICLE OPEN ACCESS

Enhanced Spectral Range of Strain-Induced Tuning of Quantum Dots in Circular Bragg Grating Cavities

Ivan Gamov[1,2] | Matthias Sauter[1] | Samuel Huber[1,3] | Quirin Buchinger[1] | Peter Gschwandtner[1] | Ulrike Wallrabe[2] | Sven Höfling[1] | Tobias Huber-Loyola[1,4]

[1]Physikalisches Institut and Würzburg-Dresden Cluster of Excellence ct.Qmat, Lehrstuhl Für Technische Physik, Julius-Maximilians-Universität Würzburg, Würzburg, Germany | [2]Laboratory for Microactuators, Department of Microsystems Engineering – IMTEK, University of Freiburg, Freiburg, Germany | [3]Centre for Nanosciences and Nanotechnologies CNRS, Universite Paris-Saclay, Palaiseau, France | [4]Institute of Photonics and Quantum Electronics (IPQ), Karlsruhe Institute of Technology (KIT), Karlsruhe, Germany

Correspondence: Ivan Gamov (ivan.gamov@imtek.uni-freiburg.de)

Received: 12 November 2025 | **Revised:** 25 January 2026 | **Accepted:** 28 January 2026

Keywords: circular Bragg grating | FEA | piezoelectric | quantum dots | quantum light | spectral tuning | strain-induced tuning

ABSTRACT

Tunable sources of entangled and single photons are essential for implementing entanglement-based quantum information protocols, as quantum teleportation and entanglement swapping depend on photon indistinguishability. Tunable devices are fabricated from indium arsenide (InAs) quantum dots (QDs) embedded in gallium arsenide (GaAs) nanomembranes placed on monolithic piezoelectric substrates. Circular Bragg grating (CBG) resonators enhance emission brightness and exploit the Purcell effect; however, the inclusion of CBGs reduces strain-mediated tunability compared to planar nanomembranes. A simple and effective solution is introduced: filling the CBG trenches with a stiff dielectric (aluminum oxide, Al_2O_3) via atomic layer deposition (ALD) restores up to 95% of the tunability of planar structures. Finite element analysis (FEA) confirms that the tunability loss originates from bending in the device layers due to strain relief in the CBG geometry. Lowering the stiffness of intermediate layers between the QDs and the piezoelectric actuator, such as in bonding or reflector layers, further increases strain losses in uncoated CBGs. Coated devices maintain 98%–99% strain-tuning efficiency across all simulated underlayer stiffnesses. The results demonstrate that advantageous optical cavity properties can be effectively combined with piezoelectric strain tuning, enabling scalable, bright, and tunable quantum light sources.

1 | Introduction

Photons are ideal carriers of quantum information due to their weak interaction with the environment and their compatibility with sending them through air or glass fibers with low losses [1, 2]. Among the numerous material platforms explored for creating quantum light sources [3–7], semiconductor quantum dots (QDs) are particularly promising due to their ability to provide bright, on-demand single-photon emission with high quantum efficiency and high photon indistinguishability, as well as their compatibility with scalable semiconductor nanofabrication [2, 6–10]. However, creating a bright and tunable photon source has proven to be more challenging in practice than anticipated, due to the need to simultaneously achieve high photon flux and high indistinguishability. These challenges can be effectively addressed through the integration of QDs into microcavities of different geometries. Among various cavity designs [11, 12], circular Bragg grating resonators (CBGs) provide a high Purcell factor over a broad emission range [13, 14], enhancing emission rates and enabling efficient collection of multiple QD transitions. [15, 16] The emission wavelength of QDs can be adjusted through growth conditions [17] or by choosing materials [18–20], but tuning on the device level is necessary to overcome growth fluctuations for quantum light applications. Several methods

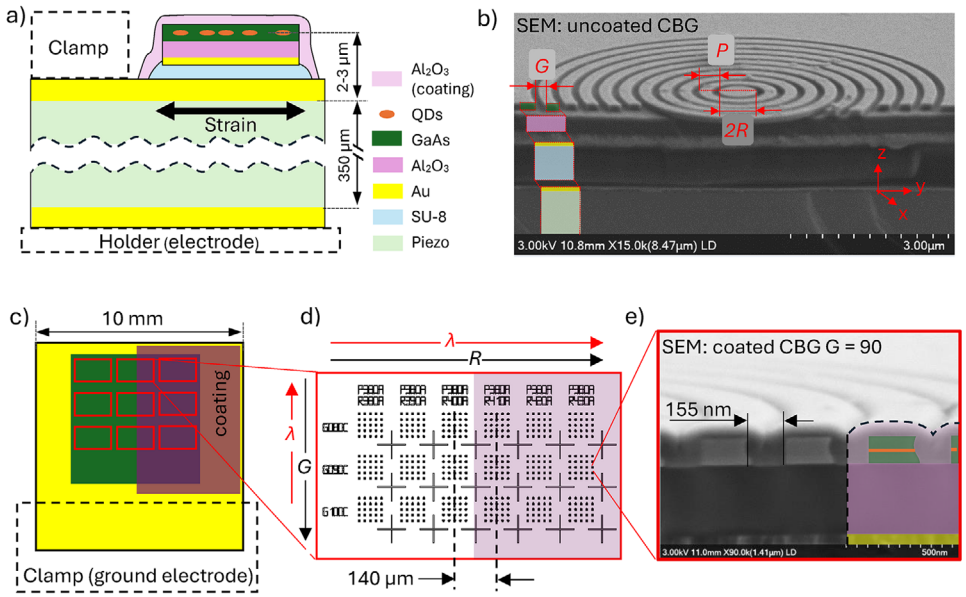

FIGURE 1 | (a) Schematic of the sample layers in the cross-section indicated by colors and (b) SEM image of a irregular fracture at uncoated CBG with coordinate system and definition of *R, P, G* processing parameters. The colored sections on the left show the local cleave in *z*-*y* plane with assumed offset along *x*-axis. (c) On the top view, the right half of the sample is coated with Al_2O_3. The CBG layout includes nine fields (red rectangles) with the same variation of the parameters. d) Each single field includes 450 CBGs at design parameter variation of *R* and *G* to control the resonance wavelength λ of the CBGs. The distance between neighboring CBGs within the same parameters (squares 5 by 5 devices) is 20 µm and the distance between the closest coated to uncoated CBGs is 140 µm. The SEM image (e) shows the cross-section of a coated CBG at design parameter $G = 90$ nm (overexposed—real gap 155 nm).

have been developed to enable spectral tunability, such as temperature tuning [7, 21, 22], optical tuning [23, 24], electric field [25–27], or magnetic field tuning [25, 28, 29]. Another approach involves strain-based spectral tuning. It allows for an extended tuning range while maintaining high photon coherence and high photon extraction probability [30–35]. Monolithic piezoelectric substrates without structuring provide both high robustness and high tunability. For thinned interfaces between the actuator and QDs, spectral shift over 10 meV (12 nm) was demonstrated [30]. Fine structure splitting (FSS) strain tuning required for multi-photon operation was shown for micromachined piezo substrates and can also be achieved with planar actuators [36]. However, strain transfer can struggle in cavity systems when the latter is not optimized for strain tuning. For example, it was shown that strain tuning in micropillar cavities is ineffective since the actuator does not transfer strain efficiently to QDs but instead the strain relaxes in the freestanding structure due to their high aspect ratio [33]. When integrating CBGs onto piezoelectric substrates, tunability has been shown [32, 33]; however, the strain transfer waned in the cavity configuration, unlike in its non-cavity counterpart.

In this paper, we demonstrate the tunability enhancement of QDs embedded into CBGs on monolithic piezoelectric substrates. Simulations of conventional CBG structures reveal a drop of tunability due to strain relief, when the etched trenches of the CBG disrupt the continuity of the monolithic membrane. On the way to a QD, over 50% of the generated strain can be lost. An additional layer of aluminum oxide (Al_2O_3) deposited on top of CBGs is shown to be an effective treatment for restoring the original high tunability of the sample in both experiment and simulation. According to measurements, the strain transfer during the actuation rises from 31% ± 4% in the standard CBGs with air trenches to 91% ± 4% when depositing Al_2O_3, relative to the tunability in the monolithic membranes (100%). Simulations of strain in both configurations (air vs Al_2O_3) help to understand the principles of the strain distribution in layers and help to find the most impactful parameters of materials in the device fabrication.

2 | Measurements of Photoluminescence Spectral Shift

The spectral shift of quantum dot photoluminescence is measured for III–V QD devices integrated with CBGs on a piezoelectric substrate for the strain-induced tuning. All tested devices were characterized at a fixed voltage, after which the applied voltage was changed to the next fixed value to induce spectral shifts of the emission. Al_2O_3 layer applied by atomic layer deposition coated one half of the sample (≈2000 CBGs). For analysis, we selected the CBGs with cavity mode in the spectral range from 880 to 920 nm and in which the trench thickness allowed coalesce of the CBG walls (i.e., complete filling of the trenches). The measurements at the closest uncoated CBGs and between CBGs provided reliable comparison of tunability. The layer configuration, devices layout, and scanning electron microscopy (SEM) images of coated and uncoated devices are presented in Figure 1 and described in the Experimental section.

The spectral shift of photoluminescence was measured for quantum dots located in both coated and uncoated regions of the sample (Figure 2). Positive voltage on the piezoelectric actuator (aligned with the poling direction) induces a blueshift of the emission peaks. Conversely, negative voltages can result in a redshift of the emission peak. Representative emission spectra are

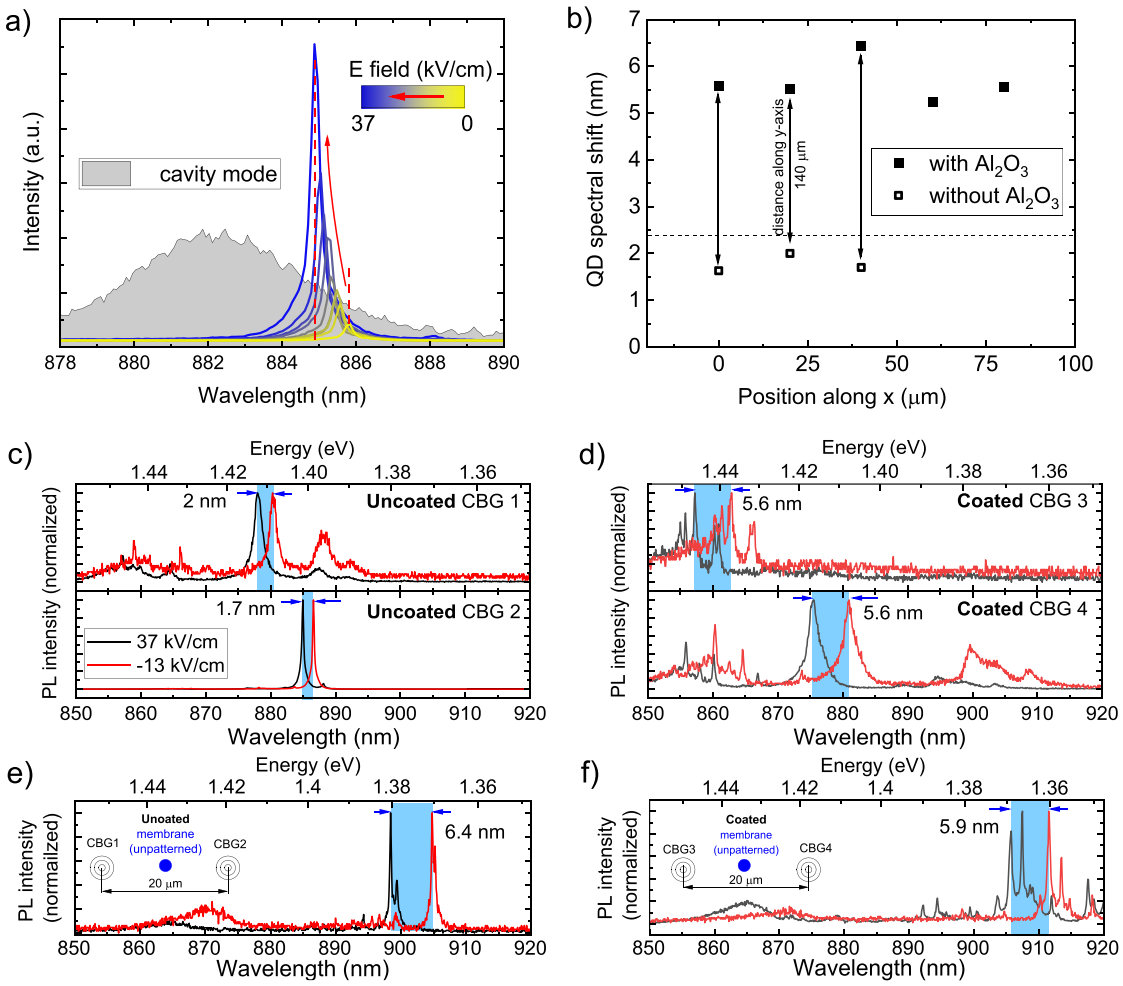

FIGURE 2 | (a) Typical photoluminescence spectra for a selected QD in uncoated CBG at different voltages. The position of the cavity mode in the white light measurements is shown in grey. (b) Maximum spectral shift at full range (50 kV cm^{-1}) actuation is shown for 8 devices from neighboring coated (filled symbols) and uncoated fields (open symbols). CBGs in this group have trenches width 130–145 nm according to SEM ($G = 80$ nm). For statistical significance we measured 10 more uncoated devices in the nearest fields; all showed spectral tuning range under 2.4 nm (dashed line). Photoluminescence spectra from (c) CBG1, CBG2, and (d) CBG3, CBG4 are shown at two extreme voltages on the piezoelectric actuator. Additional spectra captured from the monolithic membrane between selected nearest devices, (e) uncoated CBG1 and CBG2, or (d) coated CBG3 and CBG4.

shown in different colors in Figure 2a only for positive voltage. In Figure 2b we show the spectral tuning range for different devices, five coated and three uncoated CBGs. These CBGs are located in the upper two fields crossed by the dashed line in Figure 1d. Selected spectra from a pair of uncoated devices (CBG1, CBG2) and a pair of coated devices (CBG3, CBG4) are shown in Figure 2c,d, respectively. Spectral shifts related to areas of monolithic membrane between corresponding devices are shown in Figure 2e,f.

All devices associated with Figure 2b–f were measured for a single cycle of static actuation in full voltage range from 37 kV cm^{-1} to −13 kV cm^{-1} to exclude the factor of piezoelectric hysteresis and variations in pre-experiment poling of the piezoelectric crystal. We checked 13 conventional devices from three neighboring fields in the uncoated region and found the tuning range to be 2.4 nm maximum and 1.73 nm in average. In the same fields, four points between CBGs showed minimum 6.0 nm and average tuning range equal to 6.48 nm. Typical spectra from unprocessed membrane between CBGs in uncoated region are shown in Figure 2e. In contrast, the two nearest CBGs (10 µm away) showed the tuning range 1.7 and 2.0 nm (Figure 2c). The nearest measured five coated CBGs (~140 um away) demonstrate average tuning range of 5.7 nm, enhanced approximately three times due to complete Al_2O_3 filling of the trenches. Two of these coated CBGs are shown in Figure 2d. We notice that at the same time the unprocessed membrane keeps high spectral tuning range under the Al_2O_3 film (cf. Figure 2f). Thus, the data set indicates the drop of the tunability for the conventional (uncoated) CBGs while the optimized (coated) cavities keep it as high as in the unpatterned membrane. The apparent variations observed between individual measurements are within the intrinsic device-to-device variability and do not indicate a systematic effect of the Al_2O_3 coating.

In addition to the widened tuning range of the QD emission in coated CBGs, the CBG cavity modes become sensitive to the piezoelectric tuning. The spectra in Figure 3a, captured for another cycle of actuation shows the cavity mode of the selected coated CBG. To specify the range of tuning, in Figure 3b we

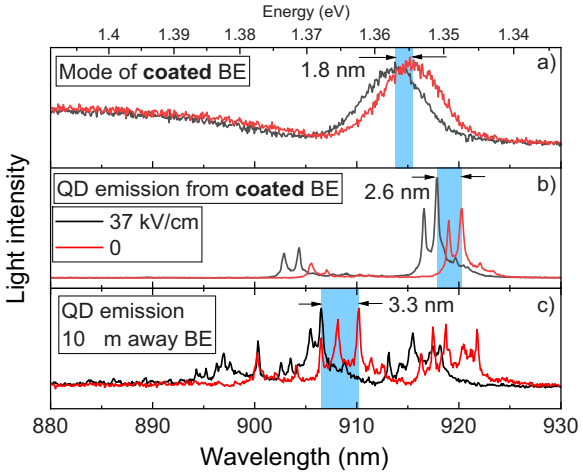

FIGURE 3 | White light spectra and QD emission from a selected CBG at 0 and 37 kV cm^{-1} applied voltage on the piezo electrodes. If compared to the spectral shift for QDs 10 μm away from the CBG (3.3 nm), the 1.8 nm blue shift of the CBG mode corresponds to 54% while the spectral shift of QD emission lines in this CBG is 79% (2.6 nm). For uncoated CBGs, the strain-induced shift stays always under 1/10 of corresponding QD tuning range (not shown).

demonstrate the QD emission embedded in the CBG, and (c) a random QDs' emission 10 μm away the CBG for this same actuation cycle. The monolithic membrane in this region of the sample shows the tuning range of 3.3 nm for the applied voltage range. The tuning range of the QD within the CBG is 2.6 nm and the shift of the CBG mode is 1.8 nm. For uncoated CBGs, the cavity mode tuning range is always under 10% of the QD's observed emission shifts. In the coated CBG, the mode tunes in the same direction as the QD, but with only 60%–70% of the slope, such that the QD can still be brought in resonance at initial detuning. A relatively small initial energy difference can be achieved by deterministic placement of the CBGs, which was not performed in this study, but is in principle possible [37–39]. The simultaneous shift of both the cavity mode and the QD emission indicates that the CBG-QD system remains coupled over a wider wavelength range during the piezoelectric tuning if compared to virtually pinned mode position in conventional CBGs.

3 | Finite Element Method Simulations

Finite element method (FEM) simulations in COMSOL Multiphysics [40] reproduce the behavior of both uncoated and coated CBG designs (Figure 4). The CBGs were simulated with the following parameters: R = 800 nm, P = 400 nm, G = 100 nm, thickness of GaAs membrane 120 nm. The materials' Young's moduli (σ) are assumed to be close to the material properties at room temperature [41–44]. We avoid numerical evaluation of absolute material deformation by normalization of all results to the probe values on the surface of the membrane away of the CBG structure on Figure 4a,b. Thus, value of 100% (shown by white/grey) of the in-plane strain component ε_{xx} spreads to most of the volume and major part of the top surface of the device except the CBG structure and the close area around it. The red (blue) coloration indicates strain accumulation (release) during the actuation, independent of whether the actuation corresponds to contraction or expansion of the piezoelectric substrate. The deformation ε_{xx} of the bulk piezoelectric material predefined by applied voltage multiplied to piezoelectric constant d_{31} was found between 101 and 103% for all simulations.

Figure 4 compares coated and uncoated devices for three different configurations of σ in the layers. The left column (Figure 4a,c,e) shows uncoated devices, while the coated ones are in the right column (Figure 4b,d,f). The case of a stiff dielectric (σ_{Al2O3} = 300 GPa) combined with a stiff glue layer in (a, b) illustrates the strain distribution in the experimental sample studied in this paper. In Figure 4c,d, we reduce σ in the dielectric coating. The gradual change of coating σ is considered in Figure 5a for the probe point (red point in Figure 4b). Since the Young's modulus of SU-8 at cryogenic temperatures is unknown to us, we assume for upper limit restriction σ_{SU8} = 10 GPa as a reasonable overestimation based on its room-temperature value of 4 GPa [42]. However, in Figure 4e,f, we consider additionally the glue layer at lower σ = 1 GPa. Finally, the cross-section view in Figure 5b depicts the distribution of ε_{xx} along the center axis of the CBG in all cases presented in previous figures; alternative thicknesses of the coating are considered in Figure 5c.

Bright blue regions in Figure 4a, visible around the trenches of the CBG pattern, indicate a strong influence of the latter on strain distribution. In particular, trenches not only induce the strain relief in the rims but also initiates a macroscopic deviation of the material from the behavior of a monolithic membrane. The strain relief in the GaAs layer in CBG is accompanied by strain accumulation in the dielectric and glue layers beneath the center of the structure. Since the red areas are always more deformed than the blue ones during contraction or expansion of the actuator, the deformation in this region is always of bending type.

The ability to bend strongly depends on the Young's modulus of underlying layers since these layers can block the out-of-plane deflection of the weaken GaAs. In coated CBGs, the GaAs weakened by trenches is compensatory reinforced by the Al_2O_3 filling; as a result, the layer does not force the bending, the CBGs tend to remain in-plane, and lowering the Young's modulus of the underlayers keeps the tuning properties essentially unchanged. Depending on the device configuration and choice of materials, the strain transfer to the center of the CBG core can be limited by 38%–61% if the QD layer is exactly in the middle of the etched depth. The efficiency can be under 30% (cf. Figure 5b), in case QDs are located closer to the top surface.

The effect of ALD Al_2O_3 coating on the strain distribution is demonstrated in Figure 4b,d,f. The probe values are in the range of 98%–99% for all considered stiffness variations. The distribution of the strain along the CBG z-axis becomes homogeneous as illustrated in Figure 5b. It confirms that the coating suppresses parasitic bending of the layers. From a practical point of view, this indicates that the QDs can be located at any depth without compromising effective tuning.

Important to notice that we see slight dependence of the strain in the core along radial coordinate also. If QDs are located far away from the center, the additional losses of tuning efficiency can occur in uncoated CBGs while it can even gain in coated

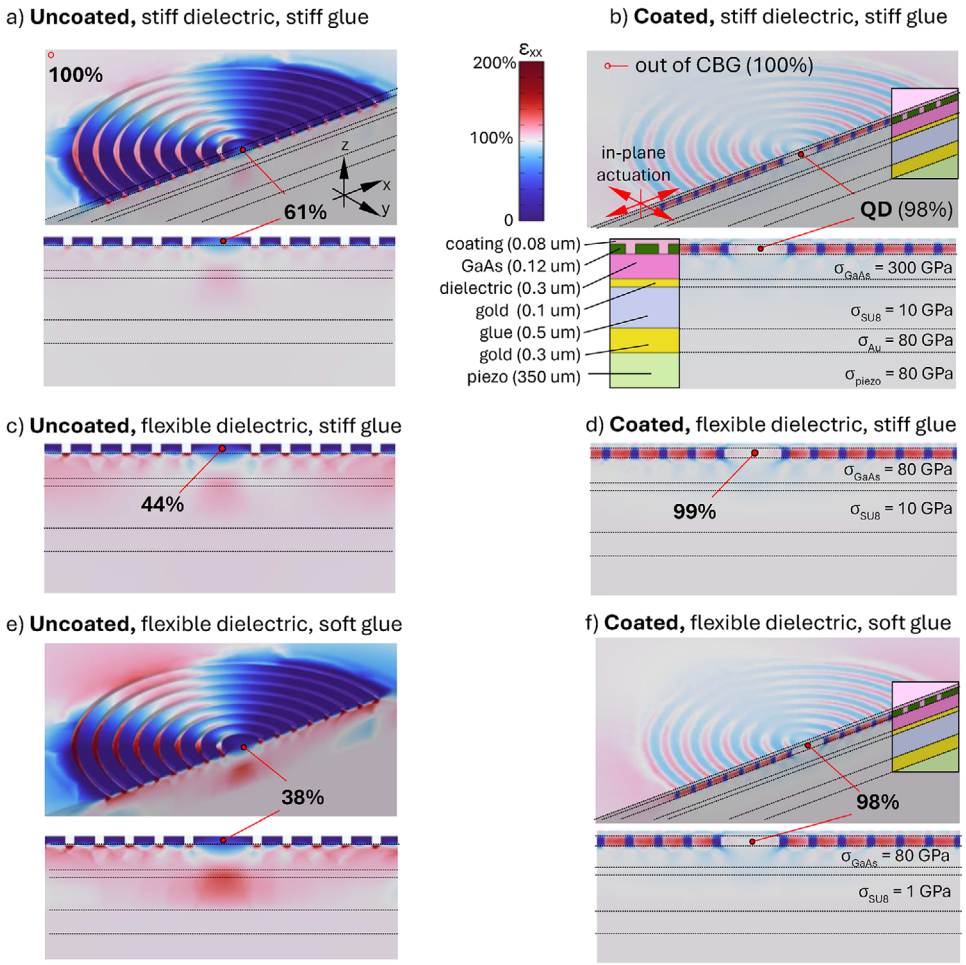

FIGURE 4 | FEM simulations of strain distribution in uncoated (a, c, e) and coated (b, d, f) CBGs. All strain values are normalized to the maximum deformation on the surface of monolithic membrane in (b) away from CBG (100% is shown in grey). The direction of the in-plane actuation is shown by arrows. The probe values (red probe point) given in % for each figure correspond to the relative strain in the core center at z in the middle of GaAs. The regions of reduced deformation (strain relaxation) appear in blue, while regions of enhanced deformation (strain accumulation) appear in red on the color maps. Compared to the configuration of materials in our measured devices (a, b), Young's modulus values between the QD and the piezoelectric substrate decreased in dielectric layer from 300 to 80 GPa (c, d) imitating behavior of SiO_2 [34] and in the glue layer from 10 to 1 GPa (e, f) imitating softer glue media.

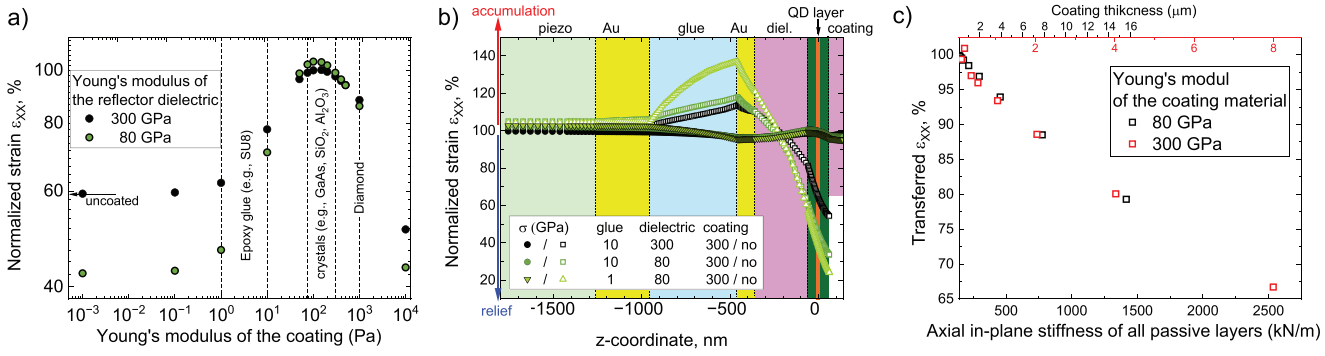

FIGURE 5 | (a) Normalized in-plane strain (ε_{xx}) versus Young's module σ of the coating material for the probe points shown in Figure 4. The values above (below) 100% correspond to strain accumulation (relief). Two different reflector dielectric materials are investigated. (b) Includes the values of ε_{xx} along the CBG symmetry axis (z-coordinate) for all the cases depicted in Figure 4. The filled (open) symbols correspond to coated (uncoated) samples; the legend contains layers' Young's moduli given in GPa. In (c) strain ε_{xx} is shown at different thickness of coating film and normalized to the strain generated by freestanding piezoelectric. The axial in-plane stiffness is calculated for the composite film comprising the passive layers on the piezo actuator. These layers are shown in the cross-section in (b).

CBGs but always stays in the range 99%–105%. Since our CBGs are fabricated in array but not deterministically, uncoated CBG can show lower tunability in the experiment due to this effect. The coating unifies the tunability along radial coordinate and brings it to the level of monolithic membrane.

In uncoated CBGs, Young's modulus in the underlayers change the resulting stress in the QD layer. Figure 4b,d demonstrates that a stiffer underlying dielectric Al_2O_3 layer causes lower losses than more flexible materials such as SiO_2 (Figure 4a,c). Both materials are conventional choice for devices [34]. At first sight, a preference of Al_2O_3 may seem counterintuitive, since by a wrong analogy to monolithic membrane, a stiff layer is expected to oppose mechanical actuation stronger. However, this logic works only for thicker films that result high total stiffness. We evaluate the in-plane axial stiffness of the passive composite layer on top of the piezoelectric substrate to quantify the possible impact of the coating film into the losses. For the thicknesses and moduli listed in Figure 4b, the stiffness of the composite film reaches 160 kN m^{-1} (or 160 GPa µm, i.e., modulus by thickness) of which only 24 kN m^{-1} are from the 80 nm Al_2O_3 coating and 90 kN m^{-1} from the 300 nm Al_2O_3 reflector dielectric. This stiffness is only 0.6% of the value for the piezoelectric bulk element. Thus, in the considered devices, the 300-nm Al_2O_3 layer of the reflector is too thin to opposite the forces generated by the 350-µm piezoelectric substrate. Correction to cryogenic parameters of materials is required.

The passive layers considered in our models (Figure 4) naturally reduce the strain transferred to QD but no more than 2% if normalized to the deformation of piezoelectric material (see Figure 5c) predominantly due to the impact of the electrode and the reflector and just minorly due to the additional coating. Various σ of the coating material are considered in Figure 5a for two different reflector dielectrics. Only virtual materials with an unrealistically high σ above 1000 GPa could provide noticeable losses due to direct mechanical opposition at thickness of 80 nm. Very soft materials of coating also provide losses, but due to the bending mechanism as considered above. The materials with σ in the range 80–400 GPa are found to be the most effective for filling the trenches (e.g., the most of the metals or crystalline materials) and restore tunability. The key feature of the application in CBGs is the conformality of obtained filling and its refractive index, thus, materials like Al_2O_3 or SiO_2 or Indium Tin Oxide (ITO) match the best from tuning perspective.

In Figure 5c we showed how the thickness of the coating can suppress the deformation transferred to the QD for thicker layer (stiff and soft coating material at $\sigma = 300$ GPa and $\sigma = 80$ GPa). Thickness of the film was applied in the range from 80 nm to 8 µm (hard) or to 16 µm (soft coating). The data showed 34% (22%) loss for the thickest hard (soft) film while at thickness of 1 µm the overall losses are only 7% (1%) of the strain (normalized to values for freestanding piezoelectric actuator).

We see good agreement of the calculated and measured efficiency of the actuation. Overall, we may recommend stiffer layers beneath the membrane and above the piezoelectric for conventional CBG devices. The Al_2O_3 top coating solves two problems simultaneously: it minimizes the losses on strain transfer and makes the stiffness of underlayers virtually unrelated to the efficiency of the device tuning. Noticeably, significant losses appear due to the bending-like deformation of CBGs however, the coating itself does not oppose the actuator due to neglectable thickness relative to the piezoelectric substrate.

4 | Conclusions

In conclusion, coated CBGs represent an appropriate choice of cavities for piezoelectric strain tuning. Al_2O_3 coating of devices provides enhanced spectral tunability of QD emission compared to conventional CBGs. FEM simulations indicate that the strain distribution along the depth in the optimized coated CBGs closely resembles that of a monolithic membrane. Experimentally, the strain-induced spectral shifts in coated CBG devices reach 91% ± 4% of the shifts observed in monolithic layers.

In contrast, standard CBGs without coating show a pronounced reduction in tunability. FEM predicts a drop by a factor of 2 when stiff glue and reflector underlayers are used, and by a factor of three for softer configurations. Noticeably, the coating up to 1 µm does not opposite to thick piezoelectric. As shown, strain relief on the material's edges in the CBG rings and core causes parasitic bending in the device layers. This causes the leak of strain in the middle of the CBG core. The experimental data confirm a reduction by about a factor of 3. The simulations further clarify that the stiffness of glue and reflector layers strongly affects uncoated devices but has little influence in coated CBGs or monolithic membranes. Finally, the dielectric coating also modifies the behavior of the CBG cavity modes. In coated devices, the cavity mode shifts in the same direction as the QD emission, covering 60%–70% of its tuning range. In uncoated CBGs, the range remains below 10%. This correlated tuning of emitter and cavity mode may be exploited in applications requiring spectral alignment across multiple devices, for instance in multi-party interference experiments in quantum networks.

5 | Experimental

A 125 nm thick GaAs membrane (dark green in Figure 1a) with QDs in the middle of the layer is grown on a GaAs substrate by molecular beam epitaxy (MBE). Then a dielectric spacer layer of Al_2O_3 and a gold layer acting as a back reflector are applied using sputter deposition and evaporation. Next, the sample is transferred to a piezoelectric substrate via a flip-chip process, and the original GaAs wafer is removed by lapping and chemical wet etching. The piezoelectric substrate is a commercially available lead magnesium niobate-lead titanate (PMN-PT) monocrystalline piezoelectric with a nominal piezoelectric constant d_{33} in the range of 1800–2000 pm V^{-1} at room temperature (corresponding to $d_{31} \sim 800$ pm V^{-1}). The choice of material is reasoned by high piezoelectric coefficients compared to alternatives [45]. Cr/Au layers, referred to as electrodes, with a thickness of 10/300 nm are deposited on the 350 µm PMN-PT substrate to apply voltage. Prior to the experiment, the PMN-PT was poled at room temperature [46] with a positive polarity along with the (001) orientation of the crystal to provide biaxial stress application.

SU-8 (light blue in Figure 1) is employed for bonding; its thickness varies between 0.5 and 0.9 µm in different sample areas.

Subsequently, we use electron beam lithography and inductively coupled plasma etching to pattern the CBGs (Figure 1b) in the membrane. The CBGs are fully etched through the membrane. Finally, another Al_2O_3 layer (coating) 82 nm thick is applied via atomic layer deposition (ALD), covering only the right half of the sample (see Figure 1c, d, e) while the left half was protected by removable photoresist. The ALD ensures that the coating fills the etched trenches of the CBGs completely as shown in Figure 1e. The QD layer lies in the middle of the GaAs membrane at total depth of 62.5 nm beneath the top surface (144.2 nm for the coated part).

The electron beam layout consists of nine identical fields (Figure 1c) Within a single field, different parameters are changed: five various radii R (increase from left to right, from 380 to 450 nm), three various gap width parameter G (increase from up to down, from 80 to 100 nm), while the period P is fixed (380 nm). Each set of parameters is represented by 25 CBGs. An increase of R and decrease of G have provided the expected red shift of the cavity mode wavelength λ [47, 48].

The micro photoluminescence (PL) measurements are performed using a continuous wave laser at 671 nm for above-bandgap excitation and a resonant excitation of the cavity mode using a broad-band (white-light) excitation source. The signal is collected using fiber in the detection path aligned near normal incidence. The spot size from which light is collected is less than 1 μm^2 in both experiments. The laser and the white light beams were linearly polarized along the x-axis, while the emitted light reaching the collecting optical fiber was always polarized along the y-axis (Figure 1b). Using this excitation geometry the cavity mode can be resonantly excited using the white-light, which makes it easy to identify the CBG mode itself without observing QD emission. This polarization was fixed for all experiments, consequently this work does not include a polarization analysis. The laser beam was co-aligned to the collection and focused on the area matching the probing area while the white light beam was slightly tilted from the z-axis and intentionally misfocused. An additional aperture cuts excessive white light in real and k-space allowing observation of reproducible Fano-like curves [49–51]. This way, the cavity mode from selected CBGs in the white-light experiments reveals the spectrum similar to high-power pumping of QDs to fill the cavity mode, without the additional heating of the sample. An example of cavity mode as well as measured PL can be seen in Figures 2a and 3. A continuous flow helium cryostat Lake Shore Cryotronics Janis was used for holding the temperature at 4.3 K (according to the sensor in the cryostat basement).

Acknowledgements

The authors acknowledge the support of the state of Bavaria and the Federal Ministry of Research, Technology and Space (BMFTR) within Projects QR.X (FKZ: 16KISQ010) and QR.N (FKZ: 16KIS2209). This work was supported by the Vector Stiftung (Grant Number P2024-0772), Baden-Württemberg, Germany. THL and MS acknowledge financial support from the BMFTR within the Project Qecs (FKZ: 13N16272). The authors acknowledge support from Sabrina Estevam, Monika Emmerling, Silke Kuhn, and Johannes Düreth for sample preparation.

Open access funding enabled and organized by Projekt DEAL.

Funding

Bavaria and the Federal Ministry of Research, Technology and Space (BMFTR) within Projects QR.X (FKZ: 16KISQ010), Qecs (FKZ: 13N16272) and QR.N (FKZ: 16KIS2209); Vector Stiftung (Grant No. P2024-0772), Baden-Württemberg, Germany.

Conflicts of Interest

The authors declare no conflicts of interest.

Data Availability Statement

The data that support the findings of this study are available from the corresponding author upon reasonable request.

References

1. N. Gisin, G. Ribordy, W. Tittel, and H. Zbinden, "Quantum Cryptography," *Reviews of Modern Physics* 74, no. 1 (2002): 145, https://doi.org/10.1103/RevModPhys.74.145.

2. J. L. O'Brien, A. Furusawa, and J. Vučković, "Photonic Quantum Technologies," *Nature Photonics* 3, no. 12 (2009): 687–695, https://doi.org/10.1038/nphoton.2009.229.

3. Y.-M. He, G. Clark, J. R. Schaibley, et al., "Single Quantum Emitters in Monolayer Semiconductors," *Nature Nanotechnology* 10, no. 6 (2015): 497–502, https://doi.org/10.1038/nnano.2015.75.

4. J. McKeever, A. Boca, A. D. Boozer, et al., "Deterministic Generation of Single Photons from One Atom Trapped in a Cavity," *Science* 303, no. 5666 (2004): 1992–1994, https://doi.org/10.1126/SCIENCE.1095232.

5. C. Bradac, W. Gao, J. Forneris, M. E. Trusheim, and I. Aharonovich, "Quantum Nanophotonics with Group IV Defects in Diamond," *Nature Communications* 10, no. 1 (2019): 1–13, https://doi.org/10.1038/s41467-019-13332-w.

6. C. Santori, D. Fattal, J. Vučković, G. S. Solomon, and Y. Yamamoto, "Indistinguishable Photons From a Single-Photon Device," *Nature* 419, no. 6907 (2002): 594–597, https://doi.org/10.1038/NATURE01086.

7. A. Thoma, P. Schnauber, M. Gschrey, et al., "Exploring Dephasing of a Solid-State Quantum Emitter via Time- and Temperature-Dependent Hong-Ou-Mandel Experiments," *Physical Review Letters* 116, no. 3 (2016): 033601, https://doi.org/10.1103/PhysRevLett.116.033601.

8. P. Michler, A. Kiraz, C. Becher, et al., "A Quantum Dot Single-Photon Turnstile Device," *Science* 290, no. 5500 (2000): 2282–2285, https://doi.org/10.1126/SCIENCE.290.5500.2282.

9. N. Tomm, A. Javadi, N. O. Antoniadis, et al., "A Bright and Fast Source of Coherent Single Photons," *Nature Nanotechnology* 16, no. 4 (2021): 399–403, https://doi.org/10.1038/S41565-020-00831-X.

10. P. Senellart, G. Solomon, and A. White, "High-Performance Semiconductor Quantum-Dot Single-Photon Sources," *Nature Nanotechnology* 12, no. 11 (2017): 1026–1039, https://doi.org/10.1038/NNANO.2017.218.

11. J. M. Gérard, B. Sermage, B. Gayral, B. Legrand, E. Costard, and V. Thierry-Mieg, "Enhanced Spontaneous Emission by Quantum Boxes in a Monolithic Optical Microcavity," *Physical Review Letters* 81, no. 5 (1998): 1110, https://doi.org/10.1103/PhysRevLett.81.1110.

12. T. Yoshie, A. Scherer, J. Hendrickson, et al., "Vacuum Rabi Splitting with a Single Quantum Dot in a Photonic Crystal Nanocavity," *Nature* 432, no. 7014 (2004): 200–203, https://doi.org/10.1038/NATURE03119.

13. J. Scheuer and A. Yariv, "Coupled-Waves Approach to the Design and Analysis of Bragg and Photonic Crystal Annular Resonators," *IEEE Journal of Quantum Electronics* 39, no. 12 (2003): 1555–1562, https://doi.org/10.1109/JQE.2003.819548.

14. M. Davanço, M. T. Rakher, D. Schuh, A. Badolato, and K. Srinivasan, "A Circular Dielectric Grating for Vertical Extraction of Single Quantum

Dot Emission," *Applied Physics Letters* 99, no. 4 (2011): 041102, https://doi.org/10.1063/1.3615051/341462.

15. J. Liu, R. Su, Y. Wei, et al., "A Solid-State Source of Strongly Entangled Photon Pairs with High Brightness and Indistinguishability," *Nature Nanotechnology* 14, no. 6 (2019): 586–593, https://doi.org/10.1038/S41565-019-0435-9.

16. H. Wang, H. Hu, T.-H. Chung, et al., "On-Demand Semiconductor Source of Entangled Photons Which Simultaneously has High Fidelity, Efficiency, and Indistinguishability," *Physical Review Letters* 122, no. 11 (2019): 113602, https://doi.org/10.1103/PHYSREVLETT.122.113602.

17. L. Wang, A. Rastelli, and O. G. Schmidt, "Structural and Optical Properties of In(Ga)As/GaAs Quantum Dots Treated by Partial Capping and Annealing," *Journal of Applied Physics* 100, no. 6 (2006): 64313, https://doi.org/10.1063/1.2349432/370473.

18. P. Holewa, A. Reiserer, T. Heindel, S. Sanguinetti, A. Huck, and E. Semenova, "Solid-State Single-Photon Sources Operating in the Telecom Wavelength Range," *Nanophotonics* 14, no. 11 (2025): 1729–1774, https://doi.org/10.1515/NANOPH-2024-0747.

19. L. Zhai, M. C. Löbl, G. N. Nguyen, et al., "Low-Noise GaAs Quantum Dots for Quantum Photonics," *Nature Communications* 11, no. 1 (2020): 1–8, https://doi.org/10.1038/s41467-020-18625-z.

20. J. Tatebayashi, M. Nishioka, T. Someya, and Y. Arakawa, "Area-Controlled Growth of InAs Quantum Dots and Improvement of Density and Size Distribution," *Applied Physics Letters* 77, no. 21 (2000): 3382–3384, https://doi.org/10.1063/1.1327613.

21. H. Wang, Y.-M. He, T.-H. Chung, et al., "Towards Optimal Single-Photon Sources from Polarized Microcavities," *Nature Photonics* 13, no. 11 (2019): 770–775, https://doi.org/10.1038/s41566-019-0494-3.

22. S. Unsleber, Y.-M. He, S. Gerhardt, et al., "Highly Indistinguishable On-Demand Resonance Fluorescence Photons from a Deterministic Quantum Dot Micropillar Device with 74% Extraction Efficiency," *Optics Express* 24, no. 8 (2016): 8539–8546, https://doi.org/10.1364/OE.24.008539.

23. Y. He, Y.-M. He, Y.-J. Wei, et al., "Indistinguishable Tunable Single Photons Emitted by Spin-Flip Raman Transitions in InGaAs Quantum Dots," *Physical Review Letters* 111, no. 23 (2013): 237403, https://doi.org/10.1103/PhysRevLett.111.237403.

24. C. Gustin, Ł. Dusanowski, S. Höfling, and S. Hughes, "Using the Autler-Townes and ac Stark Effects to Optically Tune the Frequency of Indistinguishable Single Photons from an On-Demand Source," *Physical Review Research* 4, no. 2 (2022): 023045, https://doi.org/10.1103/PhysRevResearch.4.023045.

25. M. A. Pooley, A. J. Bennett, A. J. Shields, I. Farrer, and D. A. Ritchie, "Energy-Tunable Quantum Dot with Minimal Fine Structure Created by Using Simultaneous Electric and Magnetic Fields," *Physical Review Applied* 1, no. 2 (2014): 024002, https://doi.org/10.1103/PhysRevApplied.1.024002.

26. C. Kistner, T. Heindel, C. Schneider, et al., "Demonstration of Strong Coupling via Electro-Optical Tuning in High-Quality QD-Micropillar Systems," *Optics Express* 16, no. 19 (2008): 15006–15012, https://doi.org/10.1364/OE.16.015006.

27. R. B. Patel, A. J. Bennett, I. Farrer, C. A. Nicoll, D. A. Ritchie, and A. J. Shields, "Two-Photon Interference of the Emission from Electrically Tunable Remote Quantum Dots," *Nature Photonics* 4, no. 9 (2010): 632–635, https://doi.org/10.1038/NPHOTON.2010.161;SUBJMETA.

28. L. Sapienza, R. Al-Khuzheyri, A. Dada, A. Griffiths, E. Clarke, and B. D. Gerardot, "Magneto-Optical Spectroscopy of Single Charge-Tunable InAs/GaAs Quantum Dots Emitting at Telecom Wavelengths," *Physical Review B* 93, no. 15 (2016): 155301, https://doi.org/10.1103/PHYSREVB.93.155301/FIGURES/4/MEDIUM.

29. R. M. Stevenson, R. J. Young, P. See, et al., "Magnetic-Field-Induced Reduction of the Exciton Polarization Splitting in InAs Quantum Dots," *Physical Review B* 73, no. 3 (2006): 033306, https://doi.org/10.1103/PhysRevB.73.033306.

30. R. Trotta and A. Rastelli, "Engineering of Quantum Dot Photon Sources via Electro-Elastic Fields," *Engineering the Atom-Photon Interaction* (Springer Nature, 2015): 277–302, https://doi.org/10.1007/978-3-319-19231-4_10.

31. Y. Chen, J. Zhang, M. Zopf, et al., "Wavelength-Tunable Entangled Photons from Silicon-Integrated III–V Quantum Dots," *Nature Communications* 7, no. 1 (2016): 1–7, https://doi.org/10.1038/ncomms10387.

32. M. B. Rota, T. M. Krieger, Q. Buchinger, et al., "A Source of Entangled Photons Based on a Cavity-Enhanced and Strain-Tuned GaAs Quantum Dot," *eLight* 4, no. 1 (2024): 1–13, https://doi.org/10.1186/S43593-024-00072-8.

33. M. Moczala-Dusanowska, L. Dusanowski, S. Gerhardt, et al., "Strain-Tunable Single-Photon Source Based on a Quantum Dot–Micropillar System," *ACS Photonics* 6, no. 8 (2019): 2025–2031, https://doi.org/10.1021/ACSPHOTONICS.9B00481.

34. M. Moczala-Dusanowska, L. Dusanowski, O. Iff, et al., "Strain-Tunable Single-Photon Source Based on a Circular Bragg Grating Cavity with Embedded Quantum Dots," *ACS Photonics* 7, no. 12 (2020): 3474–3480, https://doi.org/10.1021/ACSPHOTONICS.0C01465.

35. J. Yang, M. Zopf, and F. Ding, "Strain Tunable Quantum Dot Based Non-Classical Photon Sources," *Journal of Semiconductors* 41, no. 1 (2020): 011901, https://doi.org/10.1088/1674-4926/41/1/011901.

36. X. Yuan, S. F. Covre da Silva, D. Csontosová, et al., "GaAs Quantum Dots under Quasiuniaxial Stress: Experiment and Theory," *Physical Review B* 107, no. 23 (2023): 235412, https://doi.org/10.1103/PHYSREVB.107.235412.

37. L. Sapienza, M. Davanço, A. Badolato, and K. Srinivasan, "Nanoscale Optical Positioning of Single Quantum Dots for Bright and Pure Single-Photon Emission," *Nature Communications* 6, no. 1 (2015): 1–8, https://doi.org/10.1038/ncomms8833.

38. A. A. Madigawa, J. N. Donges, B. Gaál, et al., "Assessing the Alignment Accuracy of State-of-the-Art Deterministic Fabrication Methods for Single Quantum Dot Devices," *ACS Photonics* 11, no. 3 (2024): 1012–1023, https://doi.org/10.1021/ACSPHOTONICS.3C01368.

39. Q. Buchinger, C. Krause, A. Zhang, et al., "Deterministic Quantum Dot Cavity Placement Using Hyperspectral Imaging with High Spatial Accuracy and Precision," *Nano Convergence* 12 (2025): 36, https://arxiv.org/pdf/2505.09220.

40. COSMOL "*COMSOL Multiphysics® v. 6.2*," (COMSOL, 2025), www.comsol.com.

41. V. Klinger, T. Roesener, G. Lorenz, M. Petzold, and F. Dimroth, "Determination of Hardness and Young's Modulus for Important III–V Compound Semiconductors," *Thin Solid Films* 548 (2013): 358–365, https://doi.org/10.1016/J.TSF.2013.08.079.

42. T. Xu, J. H. Yoo, S. Babu, S. Roy, J. B. Lee, and H. Lu, "Characterization of the Mechanical Behavior of SU-8 at Microscale by Viscoelastic Analysis," *Journal of Micromechanics and Microengineering* 26, no. 10 (2016): 105001, https://doi.org/10.1088/0960-1317/26/10/105001.

43. O. Sghaier, R. Linguerri, M. Mogren, A. Mogren, S. Davis, and G. Gutiérrez, "Structural, Elastic, Vibrational and Electronic Properties of Amorphous Al_2O_3 From Ab Initio Calculations," *Journal of Physics: Condensed Matter* 23, no. 49 (2011): 495401, https://doi.org/10.1088/0953-8984/23/49/495401.

44. T. Shinoda, N. Soga, T. Hanada, and S. Tanabe, "Young's Modulus of RF-Sputtered Amorphous Thin Films in the SiO_2-Y_2O_3 System at High Temperature," *Thin Solid Films* 293 (1997): 144–148, https://doi.org/10.1016/S0040-6090(96)09107-9.

45. B. P. Bruno, A. R. Fahmy, M. Stürmer, U. Wallrabe, and M. C. Wapler, "Properties of Piezoceramic Materials in High Electric Field Actuator Applications," *Smart Materials and Structures* 28, no. 1 (2018): 015029, https://doi.org/10.1088/1361-665X/AAE8FB.

46. Q. Hu, H. Liao, X. Liu, et al., "Boosting the Piezoelectric Property of Relaxor Ferroelectric Single Crystal via Active Manipulation of Defect

Dipole Polarization," *Journal of Materiomics* 9, no. 1 (2023): 166–173, https://doi.org/10.1016/J.JMAT.2022.08.004.

47. A. Yariv and J. Scheuer, "Annular Bragg Defect Mode Resonators," *Journal of the Optical Society of America B* 20, no. 11 (2003): 2285–2291, https://doi.org/10.1364/JOSAB.20.002285.

48. T. Kupko, S. Rodt, T. Heindel, S. Reitzenstein, and L. Rickert, "Optimized Designs for Telecom-Wavelength Quantum Light Sources Based on Hybrid Circular Bragg Gratings," *Optics Express* 27, no. 25 (2019): 36824–36837, https://doi.org/10.1364/OE.27.036824.

49. M. Galli, S. L. Portalupi, M. Belotti, L. C. Andreani, L. O'Faolain, and T. F. Krauss, "Light Scattering and Fano Resonances in High-Q Photonic Crystal Nanocavities," *Applied Physics Letters* 94, no. 7 (2009): 071101, https://doi.org/10.1063/1.3080683/165800.

50. M. F. Limonov, M. V. Rybin, A. N. Poddubny, and Y. S. Kivshar, "Fano Resonances in Photonics," *Nature Photonics* 11, no. 9 (2017): 543–554, https://doi.org/10.1038/NPHOTON.2017.142.

51. K. Xiong, X. Li, Y. Wei, et al., "Efficient Generation of Single Photons by Quantum Dots Embedded in Bullseye Cavities with Backside Dielectric Mirrors," *Optics Express* 31, no. 12 (2023): 19536–19543, https://doi.org/10.1364/OE.492962.